In-situ shear-banding quantification of surfactant solutions in straight microfluidic channels

In-situ shear-banding quantification of surfactant solutions in straight microfluidic channels

Viviane Lutz-Bueno, Rossana Pasquino, Simon J. Haward, Amy Q. Shen, and Peter Fischer

---

Articles you may be interested in

In-situ shear-banding quantification of surfactant solutions in straight microfluidic channels

Viviane Lutz-Bueno[a)]

Institute of Food, Nutrition and Health, ETH Zurich, Schmelzbergstasse 7, 8092 Zurich, Switzerland

Rossana Pasquino

Department of Chemical, Materials and Industrial Production Engineering, Universitá degli Studi di Napoli Federico II, P. le Tecchio 80, 80125 Naples, Italy

Simon J. Haward and Amy Q. Shen

Micro/Nano/Biofluidics Unit, Okinawa Institute of Science and Technology, 1919-1 Tancha, Onna-son, Okinawa 904-0495, Japan

Peter Fischer

Institute of Food, Nutrition and Health, ETH Zurich, Schmelzbergstasse 7, 8092 Zurich, Switzerland

Abstract

Surfactant molecules aggregate into various micellar morphologies, depending on temperature, concentration, formulation, and flow. Micellar solutions are known to undergo shear-banding when subjected to strong shear rates, as the fluid spontaneously divides itself into bands of high and low-shear rate, both under the same applied shear stress. This phenomenon occurs because of the complex structure of micellar solutions, which undergo phase transitions upon applied flow, changing the viscosity accordingly. Here, we study shear-banding of micellar solutions in one of the simplest microfluidic geometries, a straight planar channel with rectangular cross section. Four solutions with similar zero-shear viscosity and nonlinear rheological response, but different structures are compared to investigate the flow-structure relation and its impact on shear-banding. Micellar solutions are prepared by adding different amounts of the same organic salt, sodium salicylate, to surfactant molecules with different headgroups, i.e., cetyltrimethylammonium bromide and cetylpyridinium chloride. From spatially resolved microparticle image velocimetry and flow-induced birefringence measurements, the shear rate and shear stress profiles developed on the xy-plane of a planar microchannel are obtained from a series of volumetric flow rates. Based on these profiles, *in-situ* rheological parameters, such as the local viscosity, are calculated by applying the stress-optical rule. The local response in a microfluidic channel is compared to the bulk rheological response in a rotational rheometer and clear correlations are found especially for the stress plateau region, the fingerprint of shear-banding. Based on the local rheological characterization of these micellar solutions, the development and growth of shear-bands is observed and quantified. The role of salt concentration and surfactant headgroup on the resulting micellar morphology is discussed, as well as its impact on the development of shear-banding. © *2017 The Society of Rheology*. [http://dx.doi.org/10.1122/1.4985379]

I. INTRODUCTION

Adding organic salts to an aqueous solution of cationic surfactants changes the micellar morphology from globular to rodlike, even at rest. This anisotropic growth results in solutions of long, linear, and entangled wormlike micelles (WLMs), which exhibit viscoelastic behavior. In the semidilute concentration regime, for 0.5–5 wt. % of surfactant [1], the addition of salt changes the viscoelastic network, from simple entangled WLMs to entangled branched WLMs, and finally to a multiconnected saturated network [2]. These structural changes are reflected by plotting the zero-shear viscosity η_0 as a function of molar ratio R, defined as the ratio between salt C_{salt} and surfactant concentration C_{surf}. These so-called salt-curves typically display two characteristic peaks in $\eta_0(R)$. The rheological response around the first maximum in $\eta_0(R)$ is Maxwell-like with a single relaxation time [3,4]. For this regime, the micellar reptation time λ_{rep} is much longer than their breaking and recombination times λ_{break}, thus all micelles, even with distinct lengths, relax within the same terminal relaxation time λ_t. The morphology and dynamic behavior of WLM solutions around the second peak of $\eta_0(R)$ remains unclear. A significant difference between WLMs and regular polymers is that the length of WLMs depends on surfactant concentration.

a)Author to whom correspondence should be addressed. Present address: Swiss Light Source, Paul Scherrer Institute, PSI Villigen, Switzerland. Electronic mail: viviane.lutz-bueno@psi.ch

Viscoelastic micellar solutions show unusual properties when subjected to flow, such as shear-thinning, shear-thickening, shear-banding [5], shear-induced phase transitions [6], and mechanical and elastic instabilities [7]. Semidilute WLM solutions shear-thin, when flowing through rectangular rectilinear microchannels. Haward *et al.* [7] and Lutz-Bueno *et al.* [8] observed "jets" of high velocity fluid fluctuating in stagnant fluid regions at moderate flow rates. This instability remained unstable in timescales of hours. All these nonlinear rheological behaviors are responses of the structure of the fluid (microscopic properties) to applied flow fields (macroscopic properties) [9]. For example, an imposed shear rate $\dot{\gamma}$ can stretch or break WLMs, entangle or disentangle the micellar network, or increase their length [10]. This affects the local shear stress τ, and consequently the local viscosity η of the sample. The incorporation of microscopic and macroscopic fluid properties into models remains a challenge in soft matter research [9,11].

Shear-banding is one of the most intriguing flow instabilities, as WLM solutions develop shear and structural inhomogeneities. Manneville [12] reviewed the experimental methods used to visualize and quantify shear-banding. Theoretical models assume that shear-banding has different origins such as shear-induced micellar alignment [13], micellar breakage [14,15], and phase transitions [16]. As a result, the length size distribution of WLMs under flow depends on fluid morphology, surfactant concentration, and on global flow kinematics.

According to surfactant concentration C_{surf}, three mechanisms are reported to explain shear-banding: (i) Flow-induced concentration fluctuations that enhance the diffusion of WLMs from an aligned, low-viscosity phase toward an isotropic, viscous phase for concentrated WLMs, at $C_{surf} > 20$ wt. % [1,17]. The extension of long WLMs causes their disentanglement, which drives diffusion toward the entangled, concentrated region. (ii) Opposite concentration gradients are expected in isotropic-aligned phase transitions, since the low-viscosity aligned phase is more concentrated than its coexistent high-viscosity isotropic phase [18]. In cases (i) and (ii), concentration fluctuations are directly related to mechanical instabilities [16]. (iii) For semidilute WLMs, at 0.5 wt. % $< C_{surf} < 5$ wt. %, steady shear-banding is expected [1]. Here, high shear-bands are composed by flow-aligned, low-viscosity and low entanglement density WLMs, which coexist with low shear-bands composed of highly entangled, isotropic WLMs [18].

In microfluidics, shear-banding of WLMs should include "nonlocal effects" that come from differences between bulk and microfluidic rheology attributed to diffusive terms applied to stress or shear rate [9,14,15,19]. However, a clear connection between nonlocal effects and flow instabilities remains challenging in experimental and theoretical work [9]. Masselon *et al.* [20,21] investigated the dependence of nonlocal effects on boundary conditions such as channel depth and wall roughness. They determined that wall shear rate is not affected by gap size (channel thickness), while smaller gap sizes reduce the stress plateau magnitude, calculated from kinematic measurements of velocity profiles. To know the boundary conditions of a system is fundamental, as

different slip velocities and wall shear stresses can develop. These factors directly impact the normal stress and shear stress differences between the shear-bands, causing them to be dependent on flow geometry.

At rest, most optically transparent complex fluids have isotropic structure. Imposed stress causes structural anisotropy and consequently, optical anisotropy, known as flow-induced birefringence (FIB) [22]. Velocity profile measurements are often employed to investigate shear-banding, although they do not provide information on nonlocal effects, resulting from spatial inhomogeneities. The combination of FIB and micro-particle image velocimetry (μPIV) provides essential information to couple macroscopic and microscopic fluid properties. The semiempirical stress-optical rule $\Delta n = C\Delta\tau$ relates the principal stress difference $\Delta\tau$ to the principal indices of refraction difference, known as birefringence Δn [23]. A coefficient of proportionality, called stress-optical coefficient C, is normally constant for a given fluid, varying only slightly with temperature and concentration [2,22]. Conventionally for WLMs, C is negative, as the orientation of individual surfactant molecules is perpendicular to the long axis of a micelle [2]. As birefringence depends on the local shear stress and shear rate applied to a fluid, measurements of optical anisotropy are spatially resolved. A stress-small-angle neutron scattering (SANS) rule similar to the stress-optical rule was derived by Helgeson *et al.* [24] to directly correlate rheological response to SANS anisotropy. In both cases, only linear regimes could be described, since both rules fail when nonlinearity, such as shear-banding, dominates the flow-field. As a consequence, FIB provides information about molecular alignment and how a material is stretched under flow.

In general, the stress-optical rule has been found to hold at shear rates below the onset of shear rate dependent viscosity [22] such as shear-thinning or shear-banding fluids [2]. Lerouge and Berret [6] attributed this behavior to deviations from Gaussian chain statistics. Stress-optical constant C measurements usually average over the gap of a Couette geometry for a relatively long period of time [22]. Therefore, the properties related to shear-banding are also spatially and temporally averaged and these data become insensitive to such phenomenon. Pathak and Hudson [25] measured the optical anisotropy of WLMs flowing into a shallow cross-slot microfluidic channel. They observed a critical shear rate, when the stress-optical rule fails, is lower for extensional flow compared to shear flow. Later, Haward and McKinley [26] investigated the effects of salt concentration and shear-banding on the optical anisotropy of WLMs. Ober *et al.* [22] compared FIB of a shear-thinning solution of cetyltrimethylammonium bromide (CTAB) and sodium salicylate (NaSal) ($R = 8$) to a shear-banding solution of cetylpyridinium chloride (CPyCl) and NaSal ($R = 0.6$). The shear-banding solution formed regions of localized, high optical anisotropy near the walls, while the shear-thinning solutions exhibited smooth variations across channel width even with increasing flow rates.

Decruppe and Ponton [2] investigated the rheological and optical properties of four solutions of cetyltrimethylammonium chloride (CTAC) and sodium salicylate (NaSal) within a molar ratio range of $R = 0.51$–3.4 to adjust the zero-shear

viscosities to $\eta_0 \approx 18\,\text{Pa s}$. They noticed similar optical and rheological behaviors for solutions with $R > 1$, when subjected to low shear rates in Couette cells. They concluded that the micellar structures of these solutions, based on their rheological and optical properties, do not depend on salt concentration. However, we note that the shear rates were maintained relatively low $\dot\gamma = 5\,\text{s}^{-1}$. Here, we expand those results as we investigate the interdependence between mesoscopic structure and confined flow of WLMs in straight microfluidic channels at shear rates up to $\dot\gamma = 10^4\,\text{s}^{-1}$, focusing on techniques to observe the development of shear-banding [22]. Four WLM solutions with similar zero-shear viscosity $\eta_0 \approx 100\,\text{Pa s}$ are selected to investigate the effect of electrostatic screening on shear-banding as we maintain the surfactant concentration constant at 100 mM, while changing the amount of NaSal. This complements our previous studies of WLMs at rest, covering the atomic scale and focusing on electrostatic interactions between different headgroups with NaSal [27,28]. Here, the local shear rates are measured by μPIV and the corresponding local stresses are measured by FIB. We develop a method to obtain a spatially resolved map of the local viscosity. This enables us to demonstrate how micellar morphology differs, according to sample formulation and flow field, as the stress response results from the application of strong deformations, which impact the viscoelasticity of the fluid through shear-banding. Finally, a modification of the stress-optical rule enables us to estimate not only the local viscosity but also correlations to the normal stress as a function of imposed flow rate. Apart from the kinematics of WLMs flowing in microfluidic channels, the coupling between imposed deformation and fluid response and its impact on micellar structure are investigated.

II. EXPERIMENTAL

A. Sample preparation

Solutions of 100 mM CTAB or 100 mM CPyCl in ultrapure water (Milli-Q A10) were adjusted to $\eta_0 \approx 100\,\text{Pa s}$ by the addition of sodium salicylate, NaSal, with molar ratios $R = C_{NaSal}/C_{surf}$ of R1 = 0.35, R2 = 0.65, R3 = 0.90, and R4 = 1.50 similarly to Decruppe and Ponton [2]. All solutions had surfactant concentrations of about 3.6 wt. %, which is within the semidilute regime of $0.5 < C_{surf} < 5\,\text{wt. \%}$ [1]. All materials were purchased from Sigma Aldrich and used without purification. The samples were thoroughly mixed with a magnetic stirrer under 40 °C for at least 2 h and left to stabilize for a week before any measurement. The samples were stored in a dark environment under 22 ± 1 °C.

B. Methodology

1. Rheology

Steady shear and dynamic oscillatory measurements were performed in a stress-controlled rheometer (MCR300, Anton Paar) using a 50 mm diameter and 1° angle cone-plate geometry (CP50-1). The shear rate $\dot\gamma$ and shear stress τ are nearly uniform in this geometry, thus the viscosity $\eta(\dot\gamma)$ and first normal stress difference $N_1(\dot\gamma)$ can be readily measured, if shear-banding does not occur. These measurements were limited to relative low shear rates because of the departure from viscometric flow at higher rates. A microfluidic viscometer (m-VROC, RheoSense) equipped with a chip with a width of 3 mm and a thickness of 100 μm (C10) was used to determine the high shear rate response for $\dot\gamma > 10^4\,\text{s}^{-1}$. The pressure drop ΔP was corrected by Weissenberg-Rabinowitsch-Mooney equation [29]. All measurements were performed at 22 ± 1 °C. For dynamic measurements, the linear viscoelastic regime was determined from a strain sweep employing the same cone-plate geometry. Deformations of 5% were applied for the frequency sweeps, covering a range of frequencies ω from 100 to 0.01 rad/s. The extended Maxwell's model was fitted to storage G' and loss moduli G'' to determine the single terminal relaxation time λ_t, plateau modulus G_0, and high frequency viscosity η_∞. The terminal relaxation time λ_t is given by the geometric mean of micellar breakage time λ_{break} and micellar reptation time λ_{rep}, as in $\lambda_t = (\lambda_{break}\lambda_{rep})^{1/2}$, where λ_{break} is the inverse of the frequency at the minimum in $G''(\omega)$ [13].

2. Microfluidic setup

To compare bulk and microfluidic rheology, straight planar microchannels are employed, as discussed in [22]. Channels were produced out of glass following the microfabrication process described in [28], with the modification that two glass slides were used as walls instead of polyimide film and microscope cover slip. The same planar straight channel with thickness $t = 100\,\mu$m, width $w = 300\,\mu$m and length 3.2 cm was used for all experiments. The aspect ratio w/t of the channel is about 3. All measurements were collected at the midplane of the channel thickness $z \approx 50\,\mu$m. A fixed region of interest (ROI) was defined at $x \approx 1.6$ cm downstream, at the same distance from inlet and from outlet to avoid entrance and exit effects as shown in Fig. S1(I) [30]. The experiments were performed at room temperature 22 ± 1 °C. A glass syringe (Hamilton Gastight) was coupled to a Nemesys syringe pump (Cetoni GmbH) and connected to the microfluidics channel through Tygon tubing with inner diameter of 0.7 mm.

3. μPIV

The samples were seeded with 0.01 wt. % of fluorescent particles with diameter of 2 μm (Invitrogen). The μPIV system (TSI Instruments) consisted of a complementary metal-oxide semiconductor camera, an inverted microscope with 10×0.3 NA objective, and an Nd:YLF double-pulsed laser. Steady flow velocity profiles were averaged over 50 consecutive image pairs using conventional cross-correlation PIV algorithm (TSI Insight) with an interrogation area of 32×32 pixels. Figure S1(II-a) exhibits an example of the obtained velocity flow-field $U(x, y)$ for a ROI on the xy-plane. The measurement depth dz is defined by the depth of field of the objective [31]. For $10 \times$ objective and 2 μm particles, dz is about 39 μm or approximately 40% the channel depth.

4. Flow induced birefringence FIB

Spatially resolved retardance $\delta(x, y)$ of WLM solutions under flow was measured in microfluidic channels with a birefringence imaging system Exicor Microimager (Hinds instruments). We obtained quantitative measurements of the same xy-ROI, as shown in Fig. S1(III-a). The measurements were performed at room temperature $22 \pm 1\,°C$ with a light-emitting diode with a wavelength of $\lambda = 475$ nm. An objective of $10\times$ provided a field of view of 1×1 mm^2 with spatial resolution of approximately $0.5\,\mu m$/pixel. All measurements were performed at $z \approx 50\,\mu m$. The retardation magnitude is given by $\delta = \Delta n t$, where Δn is the birefringence and t is the sample thickness. Δn derives from the orientation of individual surfactant molecules perpendicular to flow and to the long micellar axis [2]. Values of $\delta(x, y)$ were averaged along the flow direction to obtain $\delta(y)$ as shown in Fig. S1(III-b). The background was corrected for residual retardance from the optical train by obtaining an image of the channel filled with fluids at rest. The retardance of the channel itself was $\delta \approx 0.01$ nm, much lower than the retardance of the samples measured under flow [see Fig. S1(III)].

III. RESULTS AND DISCUSSION

A. Selection of the samples

The salt-curves, i.e., zero-shear viscosity η_0 of CTAB and CPyCl as a function of molar ratio $R = C_{NaSal}/C_{surf}$ are shown in Fig. 1 [27,32]. The addition of an organic salt, such as NaSal, changes the packing parameter of WLMs, as it increases the electrostatic screening between surfactant headgroups. As a consequence, long flexible linear WLMs are formed through anisotropic micellar growth. Four solutions with similar η_0 of 100 Pa s but molar ratios as indicated in Fig. 1 were used to study the impact of electrostatic screening on the morphology of WLMs under shear flow. Both surfactants CTAB and CPyCl have similar tail length, however, the headgroup structure differs so that the influence of headgroup geometry on flow behavior can be studied [32]. Regarding the salt c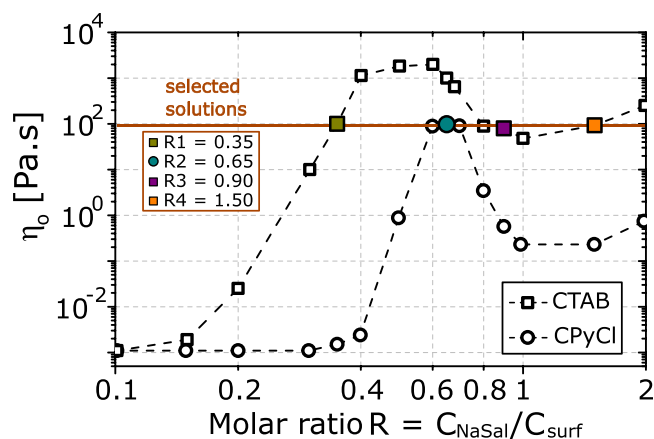ontent, R1 solution is not fully neutralized by NaSal. R2 sits on the maximum of the salt-curve, indicating a saturation point. R3 is located in the region where branched WLMs are believed to occur for surfactant/salt systems, as the viscosity decreases [33]. Finally, R4 is subjected to charge inversion, which occurs for $R > 1$, when intermicellar repulsions are again expected [34,35]. We assume two main WLM morphologies based on literature: Linear WLMs for solution R1, linear and highly entangled WLMs for R2 [22,25,26,35], branched WLMs for R3 and R4 [35,36]. In this work, we consider R4 as branched WLMs, as the structural changes leading to a second peak in $\eta_0(R)$, where R4 is located, is still unsolved [2]. We compare these different solutions under the same conditions to prove the interdependence between structure and flow upon shear-banding. As the solutions exhibit similar η_0, we assume that differences in flow behavior originate from variations in micellar morphology, mostly by electrostatic screening and micellar flexibility, both dependent on salt content and head-group structure [27,32].

B. Structure of WLMs at rest

Frequency sweeps are depicted in Fig. 2 for the selected WLM solutions. The fitting parameters for an extended Maxwell model [37]: Plateau modulus G_0, $G'(\omega)$ plateau, terminal relaxation time λ_t, and mesh size ξ are summarized in Table S1. Apart from R1, all other solutions are well described by the Maxwell model with a single relaxation time [3]. We assume that R1 deviates from the Maxwell model because of its high polydispersity not only in length but also in morphology [2]. Generally, the terminal relaxation time λ_t becomes shorter with salt addition. A similar trend is observed for the reptation time λ_{rep}. A longer reptation time indicates that longer WLMs are formed, if the solution follows a Maxwell-like behavior. As discussed, polydisperse micelles with a broad spectrum of different relaxation times are formed at low salt concentrations, having strong rheological similarities to entangled WLMs. In the case of low electrostatic screening, a broad length polydispersion could lead to the long relaxation time observed

FIG. 1. Zero-shear viscosity η_0 as a function of molar ratio R. Four surfactant-organic salt compositions were selected along $\eta_0 \approx 100$ Pa s to study the role of micellar morphology on flow development upon shear-banding.
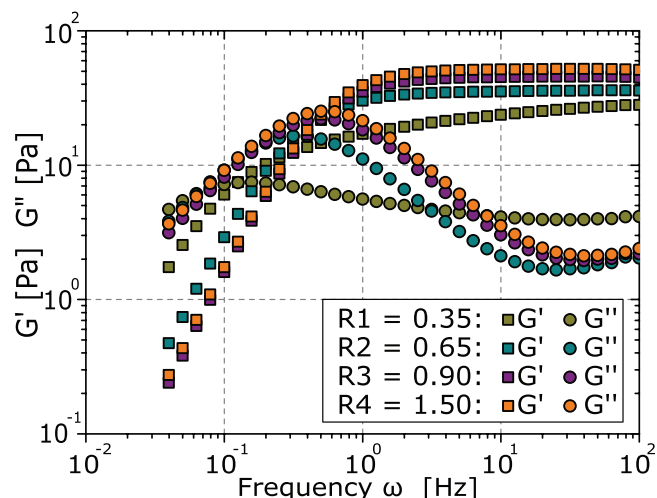

FIG. 2. Frequency sweeps in the linear viscoelastic region of the selected solutions and their identification based on molar ratio R.

for R1. No clear trend of breaking time λ_{break} as a function of R is observed. For all samples, the breaking time is the predominant factor of a monoexponential relaxation process [2]. Contrary to the relaxation times, the plateau modulus G_0 does not depend strongly on molar ratio R. The addition of salt, and consequently the electrostatic screening of the intra and intermicellar repulsions, slightly increases the magnitude of G_0 and the extension of the $G'(\omega)$ plateau. These parameters are directly related to the density of entanglements and persistence length l_p of WLMs through the mesh size ξ [38]. ξ is computed from $\xi = (k_B T/G_0)^{1/3}$, where k_B is the Boltzmann constant and T is the temperature. The addition of salt contributes only slightly to decreasing the mesh size and consequently G_0, increasing the entanglement density of the solutions. If the mesh size becomes similar to the persistence length, then an isotropic-nematic transition is expected [6].

C. Impact of flow on WLM structure

The mesoscopic structure of WLMs can be altered by flow and vice versa [9]. Here, we compare the effects of simple shear flow on the structure of the four solutions under both bulk and microfluidic flow conditions.

1. Simple shear flow under bulk flow conditions

Shear viscosity η as a function of shear rate $\dot{\gamma}$ is shown in Fig. 3(a) for all WLM solutions. In the low-shear rate regime of $\eta(\dot{\gamma})$, a Newtonian-like plateau, typical of entangled WLM solutions, is formed. However, these fluids have similar η_0 only at low shear rates $\dot{\gamma} < 0.1\,\text{s}^{-1}$. For $\dot{\gamma} > \dot{\gamma}_1$, the solutions deviate from the Newtonian behavior (see exact values of $\dot{\gamma}_1$ in Table S1). All WLM solutions shear-thin for deformation rates $\dot{\gamma}_1 \geq \lambda_t^{-1}$. In the shear-thinning region $d\eta/d\dot{\gamma} \approx -1$, viscosity is inversely proportional to shear rate [22]. R1 shear-thins at lower shear rates than the other solutions, probably due to its weaker electrostatic screening and lower structural flexibility [27]. At $\dot{\gamma} > \dot{\gamma}_2$, the solutions behave differently, since fluid elasticity is enhanced upon molecular rearrangement. The measured shear rate may differ from the true shear rate, if wall-slip, inhomogeneous or unstable flows are present. For example, it seems that R1 undergoes shear-thickening at $\dot{\gamma} > 300\,\text{s}^{-1}$ in Fig. 3(a). Figure 3(b) exhibits shear stress $\tau_{xy} = \tau$ as a function of applied shear rate $\dot{\gamma}$. In the range of $\dot{\gamma}_1 < \dot{\gamma} < \dot{\gamma}_2$, we observe a stress plateau τ_p, which is the signature of shear-banding for WLMs. The fluid divides itself into two or more bands undergoing different deformation rates, however coexisting at the same shear stress τ [22,39]. The fluid movement close to a wall arranges a phase composed by aligned micelles, which coincides with the high-shear, low-viscosity band. Simultaneously, the bulk fluid forms a high-viscosity band with nearly isotropic structure [24,40].

Solutions R1 exhibits the lowest stress plateau $\tau_p \approx 12\,\text{Pa}$ (see Table S1), but τ_p extends itself over 3 orders of shear rate in Fig. 3(b). All other solutions reach $\tau_p \approx 30\,\text{Pa}$. For $\dot{\gamma} > \dot{\gamma}_2 \approx 100\,\text{s}^{-1}$, shear stress increases again with shear rate. This increase is described by $\tau \approx \dot{\gamma}^{0.5-0.8}$, which differs from the assumption of a high viscosity branch with Newtonian-
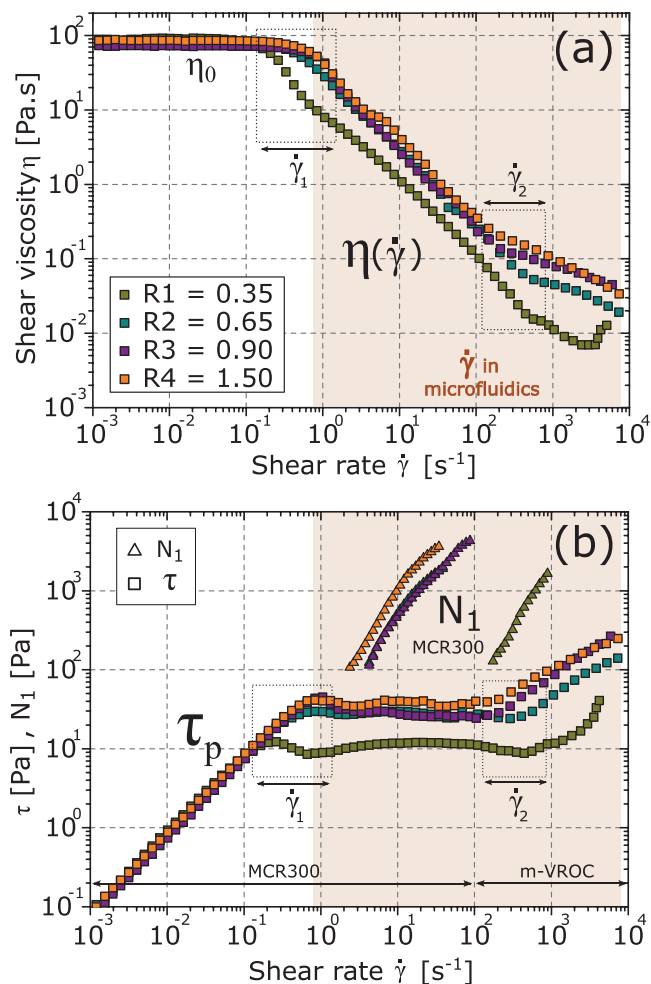

FIG. 3. (a) Steady shear viscosity η as a function of shear rate $\dot{\gamma}$ for four solutions with $\eta_0 \approx 100\,\text{Pa s}$ at low shear rates. For clarification, the shear rates in a straight microfluidic device are indicated by the shaded regions. (b) Shear stress τ and first normal stress difference N_1 as a function of shear rate $\dot{\gamma}$. The stress plateau τ_p is the signature of shear-banding. τ_p can be visualized as well as the range of its limits, $\dot{\gamma}_1$ and $\dot{\gamma}_2$. Their exact values are described in Table S1. For $\dot{\gamma} < 100\,\text{s}^{-1}$, the measurements were performed using a stress-controlled rheometer (MCR300). For $\dot{\gamma} > 100\,\text{s}^{-1}$, a m-VROC was used to avoid bulk instabilities and secondary flows at high shear rates. Note that N_1 is measured in bulk with a stress-controlled rheometer (MCR300).

like viscosity $\tau \sim \dot{\gamma}^1$ [22] (see the slopes for $\dot{\gamma} > \dot{\gamma}_2 \approx 100\,\text{s}^{-1}$ in Table S1). Only R1 shows a change in slope in the measured shear rate range. From Fig. 3(b), it is clear that not only the magnitude of τ_p depends on molar ratio but also the onset of shear-banding at $\dot{\gamma}_1$. We observe that while $\dot{\gamma}_1$ increases with the addition of salt, $\dot{\gamma}_2$ decreases (see Table S1). This causes the stress plateau region to span a progressively narrower range of $\dot{\gamma}$, as NaSal concentration and electrostatic screening increases. Shear-banding of less screened micelles occurs at lower $\dot{\gamma}_1$, where the stress plateau starts and reaches larger $\dot{\gamma}_2$ compared to more screened solutions. This indicates that shear-banding depends on how well the intermicellar interactions are screened. The low salt content of R1 and the saturation of the micellar headgroups with dissociated salt anions for R4, which occurs for $R > 1$, could lead to additional changes in morphology and flow behavior [34].

The first normal stress difference N_1, shown in Fig. 3(b), was measured by rotational rheometry only for values larger

than 100 Pa. Normal stresses are present when nonlinear viscoelastic effects occur, since they are associated with strain-induced fluid anisotropy [41], in our case resulting from micellar alignment and stretching. At high shear rates, N_1 is comparable to or larger than the shear stress [42]. Generally, all solutions show similar behavior with $N_1 \approx \dot{\gamma}^{3/2}$. At higher shear rates, the signal of $N_1(\dot{\gamma})$ becomes rather scattered and thus indicates the onset of flow instabilities in the cone-plate geometry and consequently the need of microfluidic viscometry.

2. Simple shear flow under microfluidic flow conditions

Well-defined flow fields with low Reynold number Re are generated with a straight planar microfluidic channel without inertial contributions from bulk instabilities [43]. Using straight microfluidic channel flows to investigate the onset of shear-banding in WLMs, it was shown that stratification of normal stresses is responsible for the incite of interfacial instabilities, unsteady flows, and vortices [9,22]. The calculated elasticity numbers El is in the order of 10^6, which ensures that the flow instabilities are of elastic nature and that inertial effects can be neglected compared to elastic stresses and changes in fluid structure. In the following, the flow in straight microfluidic channels is analyzed by μPIV and FIB.

a. μPIV: In-situ shear rate and banding. WLM solutions were pumped through a straight planar microfluidic channel with volumetric flow rates within $0.07 < Q < 700 \,\mu$l/min. Velocity flow profiles resulting from increasing Q are obtained by μPIV and compared in Fig. 4. In Fig. 4(a), the measured mean velocities $\langle u_x \rangle$ are shown as a function of Q and compared to the calculated $\langle u \rangle = Q/wt$. Deviations from
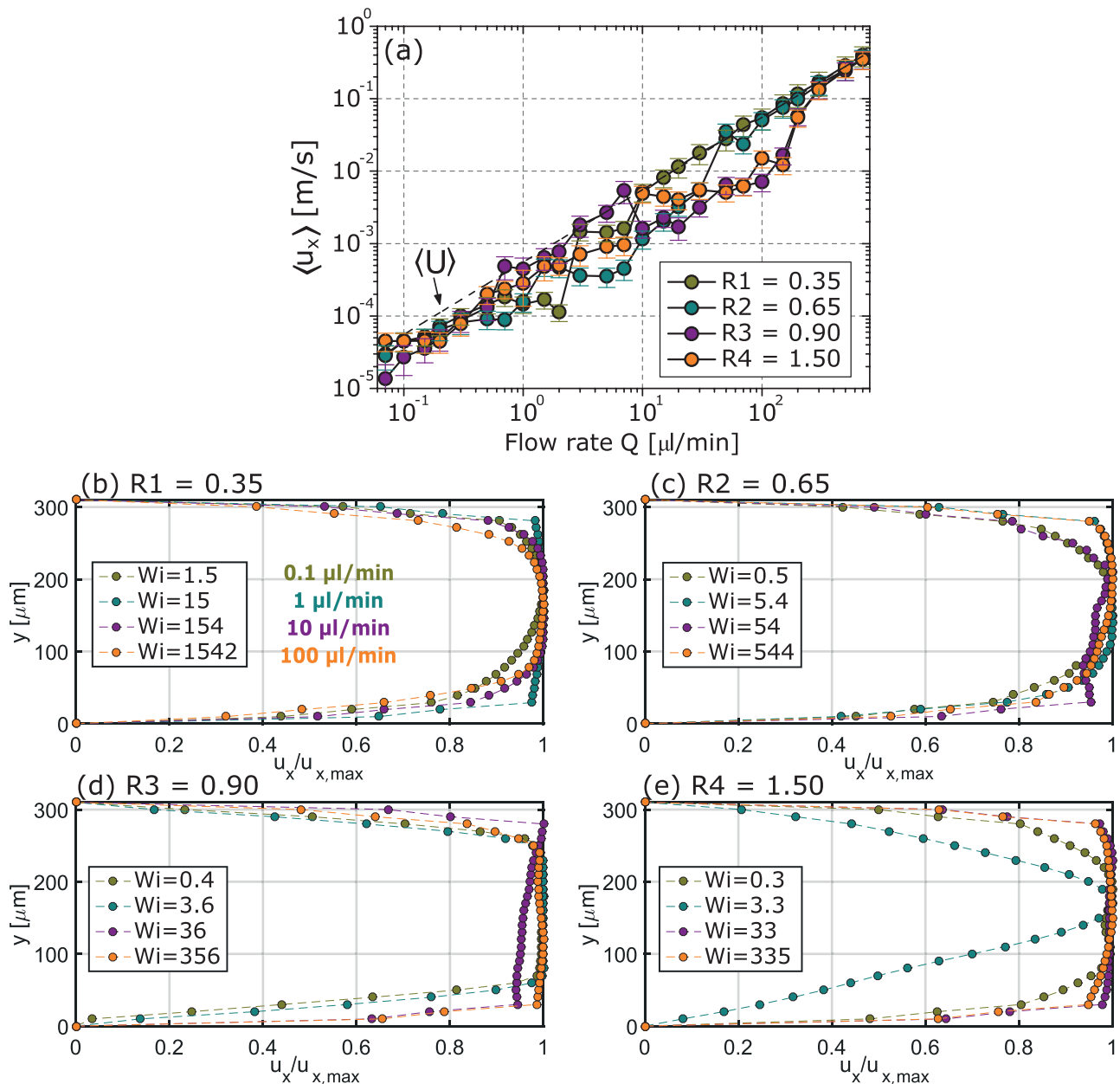

FIG. 4. (a) Mean velocity along x $\langle u_x \rangle$ as a function of flow rate Q, measured from μPIV experiments. $\langle u \rangle$ is the velocity calculated based on Q and channel dimensions. Deviations from the theoretical $\langle u \rangle$ are observed. (b)–(e) Velocity profiles of u_x along y-axis at increasing flow rate Q and Wi.

$\langle u \rangle$ are observed for $Q < 300 \, \mu l/min$, as the experimental $\langle u_x \rangle$ reaches smaller magnitudes than its theoretical equivalent $\langle u \rangle$. As measurements were performed between the midplane of the channel $z = 50 \, \mu m$ and the estimated measurement depth $dz = 39 \, \mu m$ [31], i.e., far from wall effects, possible three-dimensional flow near the walls is one of the possible explanations for these deviations. For example, it has been shown that dilute CTAB/NaSal solutions with $R = 8$ undergo shear-thinning without shear-banding while flowing through planar rectilinear microchannels. The solution exhibits varying spatio-temporally varying velocity profiles [7,22,25], indicating that WLMs develop flow instabilities with different flow patterns from those seen in homogeneous viscoelastic polymer solutions. As depicted in Figs. 4(b)–4(e), a parabolic velocity profile characteristic of Newtonian fluids becomes with increasing flow rat more and more pluglike indicating shear-thinning or shear-banding behavior: Figures 4(b)–4(e) compare four normalized flow profiles $u_x/u_{x,max}$ for flow rates Q of 0.1, 1, 10, and $100 \, \mu l/min$. The transition from parabolic to pluglike profiles occurs at a critical wall shear stress, when the Weissenberg number $Wi \approx 1$ [22,44,45].

For $Q = 0.1 \, \mu l/min$, WLM solutions R1 and R2 behave as Newtonian fluids with parabolic flow profiles [Figs. 4(b) and 4(c)]. Solutions R3 and R4 already develop pluglike profiles, characteristic of shear-thinning, even at this low flow rate and $Wi < 1$. At $Q = 1 \, \mu l/min$, R4 is the only solution developing a V-flow profile, characteristic for shear-thickening solutions [Fig. 4(e)], while R1 and R3 exhibit pluglike flow, with wider high-shear-band at the wall for R3. Shear-thickening was not observed in bulk measurements of R4 [Fig. 3(a)], probably because of the low sensitivity of the rotational rheometer for metastable states. At the same flow rate of $Q = 1 \, \mu l/min$, R2 develops an asymmetric flow profile, as it varies between pluglike and paraboliclike with x-position along the flow direction. This asymmetry in velocity profile could be originated by 3D flows along z, which cannot be resolved with our measurements of $u_x(y)$. The increase in flow rate by one order of magnitude to $Q = 10 \, \mu l/min$ causes instabilities in most of the samples. R1 goes back to a paraboliclike profile, while R2 still shows an asymmetric pluglike flow profile. R3 exhibits asymmetric pluglike profile, while R4 has a fully developed pluglike flow profile. For $Q = 100 \, \mu l/min$, R1 is the only solution exhibiting a parabolic velocity profile (Newtonian-like). This transition is characteristic of shear-thinning fluids at moderate Wi, indicating that not only shear-banding occurs. R4 displays a pluglike profile, while R2 and R3 remain asymmetric even at high Wi. Solutions R3 and R4 have similar terminal relaxation time λ_t, thus the Weissenberg numbers are also similar. Even for nearly the same Wi and zero-shear viscosity, the behavior of WLMs under high shear in a straight microfluidic channels is very distinct. The evolution of parabolic to pluglike flow profile does not follow the same trend as Wi, indicating that structure and micellar morphology play an important role on the fluid dynamics.

To compare the effects of Q on the flow profile $u_x/u_{x,max}(Q, y)$ is normalized as previously discussed in the data analysis. Figure 5 shows colormaps, where the magnitude of $u_x/u_{x,max}$ depending on channel width y and volumetric flow rate Q is mapped and represented by a color code. The colormaps of WLMs are compared to glycerol (a Newtonian fluid) under similar conditions [Fig. 5(a)]. For Newtonian fluids, flow profiles are uniform along y and are self-similar
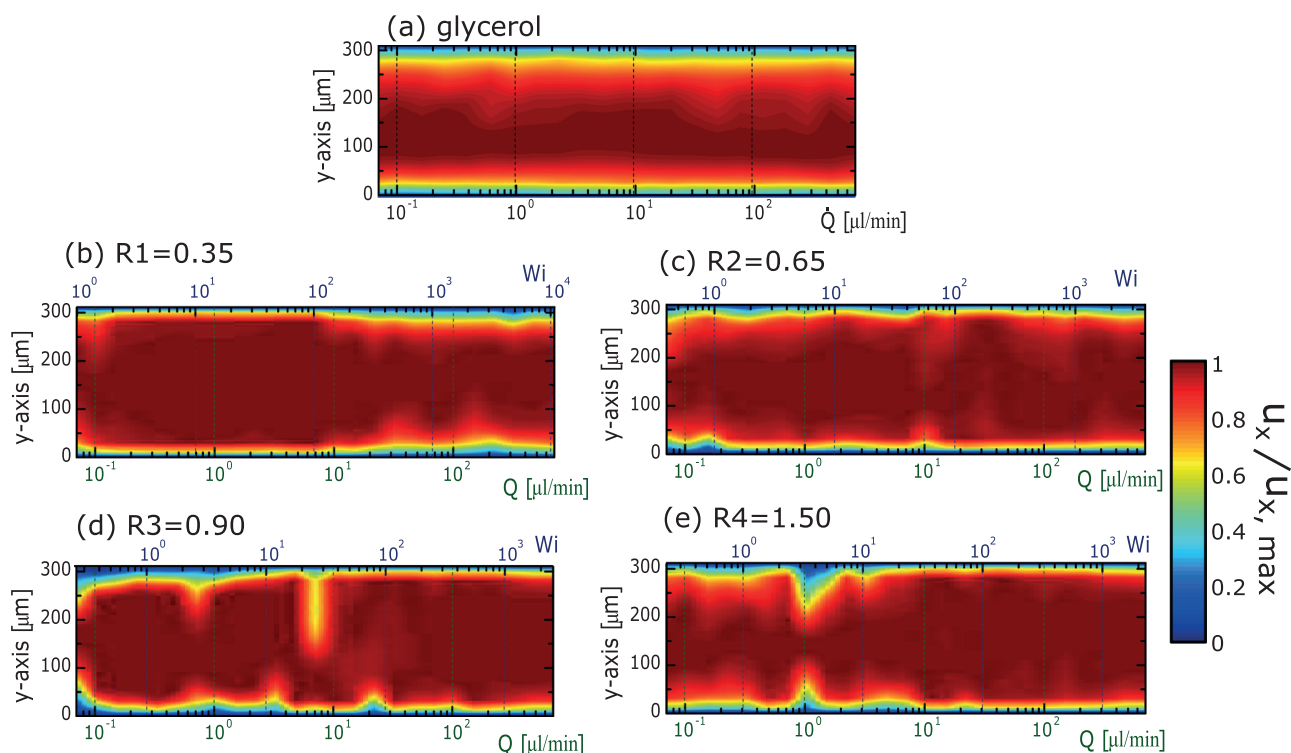

FIG. 5. Normalized representation of the velocity along the flow direction u_x divided by its maximum value $u_{x,max}$ as a function of the flow rate Q, $u_x/u_{x,max}(Q, y)$. The four selected solutions are compared to a Newtonian fluid, glycerol.

independent of the applied flow rate. This is confirmed by the constant thickness of the layers near the walls in Fig. 5(a), which represent the normalized flow profiles. As shown in Figs. 5(b)–5(e), WLMs exhibit instabilities occur with increasing Q, i.e., by changes of the color maps near the wall. These deviations from Newtonian behavior are attributed to interactions between the bulk modes of shear-banding instability and the modes associated with the interface between the bands [9]. For R1, U-shaped flow profiles are developed for $Wi > 200$, equivalent to $Q > 100$ μl/min [Fig. 5(b)]. Different behavior is observed for R2 and R3, as unstable asymmetric flow profiles between pluglike and parabolic develop, before the equilibrium for $Wi > 100$ [Figs. 5(c) and 5(d)]. A shear-thickening region can be visualized only for R4 around 10 μl/min [Fig. 5(e)]. This high salt concentration is in the same order as the typical values used for permanent gelation of WLM under high shear rates [46,47]. Although all solutions have similar zero-shear viscosities at rest, the color maps clearly suggest that the structure under flow of each fluid is different.

The flow profiles $u_x/u_{x,max}(Q, y)$ enabled us to calculate the local shear rate $\dot{\gamma}(Q, y)$ using $\dot{\gamma} = du_x/dy$. The colormaps in Figs. 6(a)–6(d) indicate the variation of the magnitude of $\dot{\gamma}(Q, y)$. The mean shear rate along y was computed for each flow rate $\langle\dot{\gamma}\rangle_{PIV}(Q)$ and compared to the calculated shear rate

$\langle\dot{\gamma}\rangle = 2\langle U\rangle/t$ as shown in Fig. 6(e). Comparing the mean value $\langle\dot{\gamma}\rangle_{PIV}$ in Fig. 6(e) for a specific flow rate Q, it is clear that the shear rates calculated locally, $\dot{\gamma}(Q, y)$, vary in orders of magnitude along y [Fig. 6(a)]. This localization of shear rates is the main characteristic of shear-banding. All studied solutions deviate from the Newtonian parabolic profile in regions where $\langle\dot{\gamma}\rangle_{PIV}(Q) < \langle\dot{\gamma}\rangle(Q)$ in Fig. 6(e). The flow rate where this deviation occurs increases with molar ratio R. The range of shear rates captured in the color map of Figs. 6(a)–6(d) is equivalent to shear-banding and shear-thinning regions in Fig. 3, indicating that these instabilities also occur in a rheometer. The selected flow rates do generate shear rates higher than $\dot{\gamma}_1$, as the lowest imposed flow rate of $Q = 0.07$ μl/min already generates wall shear rates around $10\,\text{s}^{-1}$. Additionally, the colormaps in Figs. 6(a)–6(d) indicate that high shear rate regions, developed near the walls, occur at different Wi. From Fig. 6(e), we estimate the flow rates Q_x when $\langle\dot{\gamma}\rangle_{PIV} \approx \dot{\gamma}_2$ (Table S1). Q_x are indicated in Figs. 6(a)–6(d) by the dashed lines. Note that Q_x corresponds to the mean shear rate $\langle\dot{\gamma}\rangle_{PIV}$ at the limit of the shear stress plateau τ_p, when shear-banding ends. The development of large and high shear rate regions at the walls occurs for $Q > Q_x$, while the development of pluglike flow profiles, characteristic of shear-banding, is observed for all solutions at $Q < Q_x$. The high shear regions near the walls indicate clear differences between the assumed
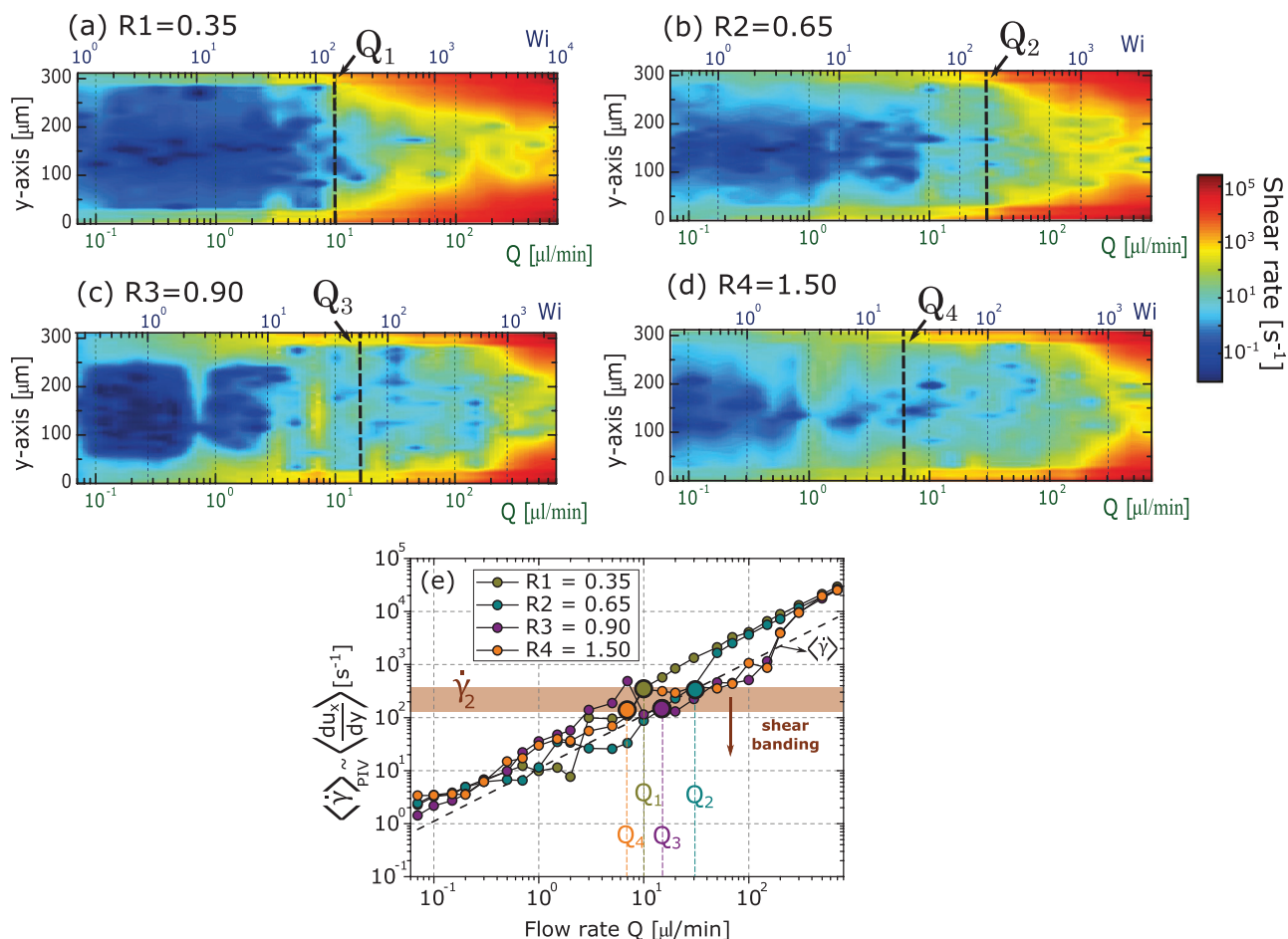

FIG. 6. (a)–(d) Shear rate $\dot{\gamma} = du_x/dy$ as a function of y and flow rate Q. The calculated shear rates for straight planar microchannels are in the order of 10^{-2}–$10^5\,\text{s}^{-1}$ for all micellar solutions. The flow rates Q_x indicate the high shear rate limit of the shear-banding region $\dot{\gamma}_2$ obtained from Fig. 3. (e) Mean shear rate $\langle\dot{\gamma}\rangle_{PIV}(Q)$ along y-axis as a function of flow rate Q. $\dot{\gamma}_2$ is indicated by the shaded region, and shear-banding is expected only for lower $\dot{\gamma}$.

linear (R1 and R2) and branched (R3 and R4) WLM solutions. R1 and R2 undergo an abrupt transition at Q_x when $Wi > 100$. Here, the high shear-bands develop into U-shaped velocity profiles. This transition also occurs for assumed branched solutions (R3 and R4), but only at $Wi > 1000$. The interface between high and low shear-bands is sharp for R1 at $Q < Q_1$. Smoother interfaces are observed for R2, R3, and R4 solutions. Masselon *et al.* [44] compared a dilute solution of CPyCl/NaSal ($R = 0.5$), which exhibited a sharp interface between shear-bands, to a dilute CTAB/NaNO$_3$ ($R = 1.35$) solution, which exhibited blurred interface. This difference was attributed to shorter self diffusion time of CTAB/NaNO$_3$ compared to CPyCl/NaSal, leading to higher concentration fluctuations at the interface and shorter correlation lengths l.

We consider that no significant concentration gradients occur during shear-banding of our measurements, as observed for semidilute concentrations [18], contrary to concentrated WLMs solutions [48]. In the case of semidilute concentration, we suggest that not only the surfactant/salt system but also the concentration of salt is essential to determine the correlation lengths l and the sharpness of the interface between the bands, as observed in Figs. 6(a)–6(d).

b. FIB: In-situ shear stress. Spatially resolved FIB measurements under the same conditions as for μPIV are shown in Fig. 7, while raw data are shown in Fig. S2 before averaging along the flow axis x. The measurements exhibit variations in retardance along the xy-plane, $\delta(x, y)$, while averaging the contributions along the channel thickness z.
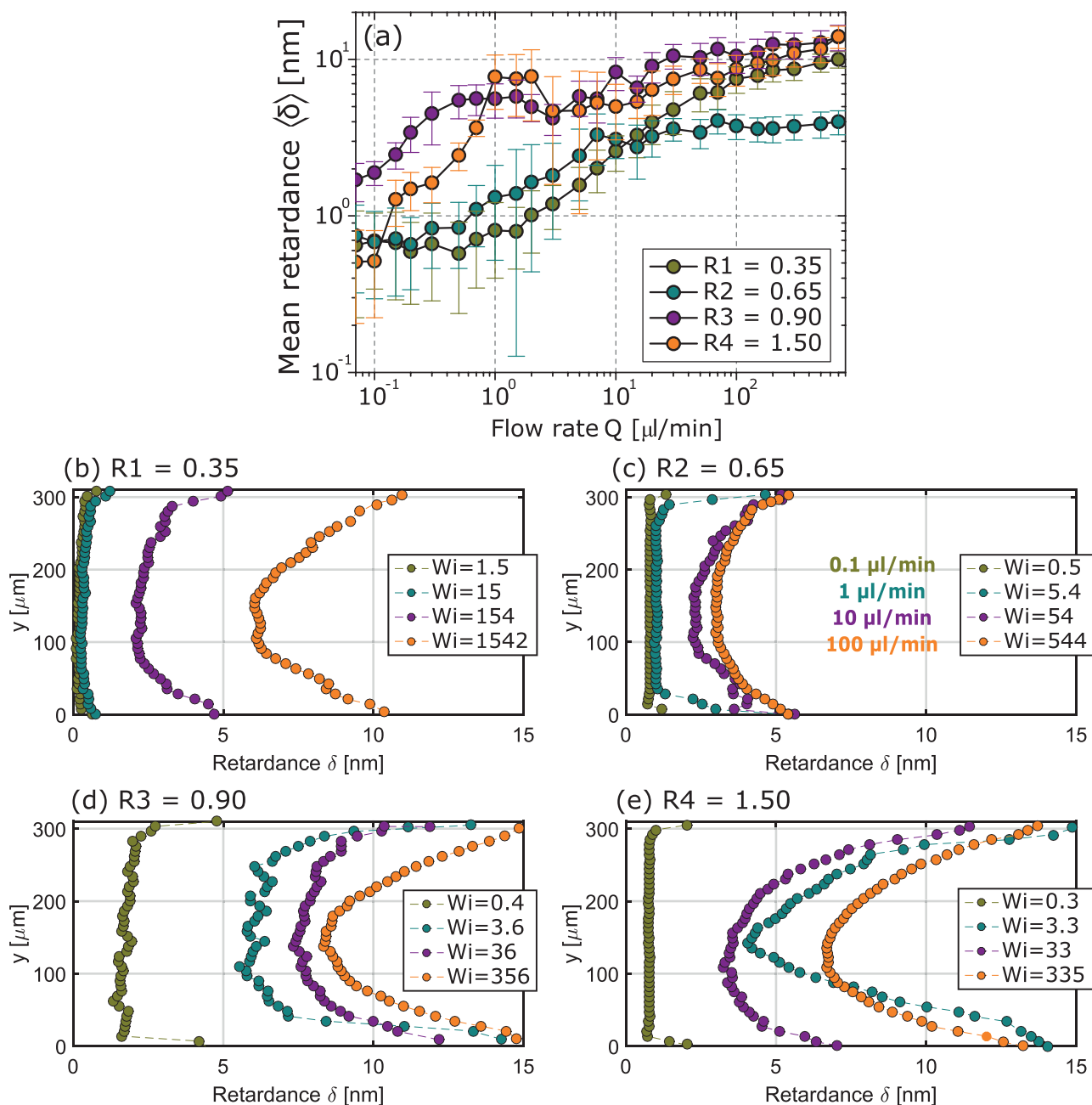

FIG. 7. (a) Mean retardance $\langle\delta\rangle$ as a function of the flow rate Q. (b)–(e) Retardance profiles δ along y-axis with increasing flow rate Q and Wi. δ is directly related to the stress in the channel.

High resolution quantitative stress distribution can be derived from spatially resolved FIB measurements, based on the stress-optical rule. Figure 7(a) exhibits the mean retardance averaged along the *xy*-plane as a function of flow rate. The trends shown by the solutions are different from the μPIV results [Fig. 4(a)]. The mean retardance $\langle\delta\rangle$ as a function of flow rate Q of linear WLMs (R1 and R2) increases within three distinct regions: (i) For low flow rates, a plateau is formed, (ii) $\langle\delta(Q)\rangle$ increases with a slope of nearly 1, and (iii) a new plateau is formed at high flow rates. For $Q > 20\,\mu$l/min, the mean retardance of R2 becomes lower than that of R1, even though the amount of salt and the density of entanglements is higher. This is explained based on the different surfactant headgroups: CTAB forms more flexible micelles [27], which align easier along the flow, undergoing deformation and generating higher retardance. $\langle\delta(Q)\rangle$ undergoes a peak around $Q \approx 0.15\,\mu$l/min, for WLMs R3 and R4. A similar instability was also observed in optical-rheometry experiments in the proximity of $\dot{\gamma}_1$, related to the formation of metastable branches during shear-banding [2,49]. The increase in retardance in Fig. 7(a) indicates a balance between Brownian motion of surfactant monomers and the action of hydrodynamical fields. The theory of rigid and long flexible particles predicts a smooth increase in retardance with flow, since the micellar entanglement reduces the rotational motion of individual micelles [2]. Here, the retardance slope as a function of flow rate increases with the amount of salt in the sample, suggesting that solutions are more entangled, confirming the mesh size ξ calculation (Table S1), derived from rheology.

The retardance profiles in Figs. 7(b)–7(e) are directly proportional to local shear stresses within the channels. The same conditions as for the experiments in Figs. 4(b)–4(e) are applied, however, the retardance profiles were not normalized to indicate the stress magnitude. If Figs. 4(b)–4(e) are compared to Figs. 7(b)–7(e) at same Q, we notice that parabolic velocity profiles usually generate pluglike retardation profiles, and vice versa. For example, sample R1 in Fig. 7(b) shows a clear transition from a flat, pluglike retardance profile to a paraboliclike retardance profile with increasing flow rate, while the opposite occurs to its velocity profiles [see Fig. 4(b)]. Similar trends are observed for measurements of R2 [compare Fig. 4(c) and Fig. 7(c)]. The assumed branched solutions (R3 and R4) undergo the already discussed peak in $\langle\delta\rangle$ as a function of Q. Before the peak, the increase in retardance is observed as the "striations" shown in Fig. S2. For WLMs R1 and R2 strong retardance is measured only near the walls for $Q > 1\,\mu$l/min, where shear rate and shear stress are maximized. For WLMs R3 and R4 undergo a striation transition, in which the stress is localized in bands, due to molecular alignment, stretching and 3D flows. These striations are observed in FIB measurements but are not detected by the velocity flow profiles measured by μPIV. This is probably due to higher spatial resolution of FIB (0.5 μm/pixel) compared to μPIV, in which the velocity field is averaged within an interrogation area of 32×32 pixels or $26.6 \times 26.6\,\mu$m^2. These striations are also observed in the retardance profiles, as shown in Figs. 7(d) and 7(e), at low flow rates, indicating the presence of structural instabilities.

Striations were previously reported by Nghe *et al.* [50], for dilute CTAB solutions during the growth of shear-bands in the *yz*-plane of straight microfluidic channels. The presence of shear-thickening for solution R4 is also observed by the V-like retardance profile for $Q = 10\,\mu$l/min, showing a good agreement between FIB and μPIV for rheological measurements.

After analyzing the retardance profiles, we apply the stress-optical rule to determine the local shear stress as a function of flow rate for WLMs in a straight microfluidic channel. Birefringence Δn was determined by dividing the retardance profiles in Figs. 7(b)–7(e) by the thickness of the microchannel $t = 100\,\mu$m. The shear stress of Poiseuille flows in the channel center (considering the *y*-dimension), which is directly proportional to the birefringence, should be zero. However, in our measurements, the birefringence in the center of the channel increases linearly with flow rate for all profiles in Figs. 7(b)–7(e). This could be related to the formation of 3D flows or high shear-bands at the bottom ($z = 0$) and top ($z = 100\,\mu$m) walls of the microfluidic channel, which we average along z in our FIB measurements of the *xy*-plane [see scheme in Fig. S1(I)]. As a correction, the minimum of the birefringence profile Δn_{min} was subtracted from the equivalent $\Delta n(y)$ at each flow rate, in order to obtain zero shear stress at the center of the channel. These values are shown in Fig. 8 multiplied by a factor of 10. The master curves in Fig. 8 describe the behavior of shear stress as a function of shear rate. The shear stress is calculated from $\tau = (\Delta n - \Delta n_{min})/C$ and plotted as a function of the local shear rate calculated in Fig. 6(e). The stress-optical coefficients C was estimated by scaling the shear stresses to the same order of magnitude as the stresses measured in a rotational rheometer (represented by dashed lines in Fig. 8) through a best fit. With the correction at the center of the channel by Δn_{min}, the stress-optical rule became valid even within the shear-banding regime, and not only for $\dot{\gamma} < \dot{\gamma}_1$, as previously reported [2,22]. The stress-optical coefficients C have the expected order of magnitude $10^{-6}\,$Pa^{-1}, if compared to rheo-optical measurements from literature [22]. The curves were not smoothed to display the deviations of shear stress from bulk rheological measurements in the shear-banding region. There are two main reasons why the stress-optical rule did not deviate within the shear-banding region of Fig. 8, as previously reported: (i) The spatial resolution and fast acquisition of FIB maps provided enough statistics to follow unsteady shear-banding flows, and (ii) FIB measurements in microchannels are spatially resolved along the velocity gradient direction, and only averaged over the vorticity direction $t = 100\,\mu$m [9], improving the spatial resolution.

The stress in the center of the channel diverges from predictions of the shear-thinning model, where $\tau = 0$. The pressure drop in microfluidic flow could be compensated by normal stresses coming from the elasticity of the fluid, as a coupling between shear-thinning, normal stresses, and memory effects [7]. As for the normal stresses, an empirical correlation between Δn_{min} scaled by the factor of 10 and the normal stress N_1 measured with a rotational rheometer was found (see Fig. 8). The correlation can be calculated by
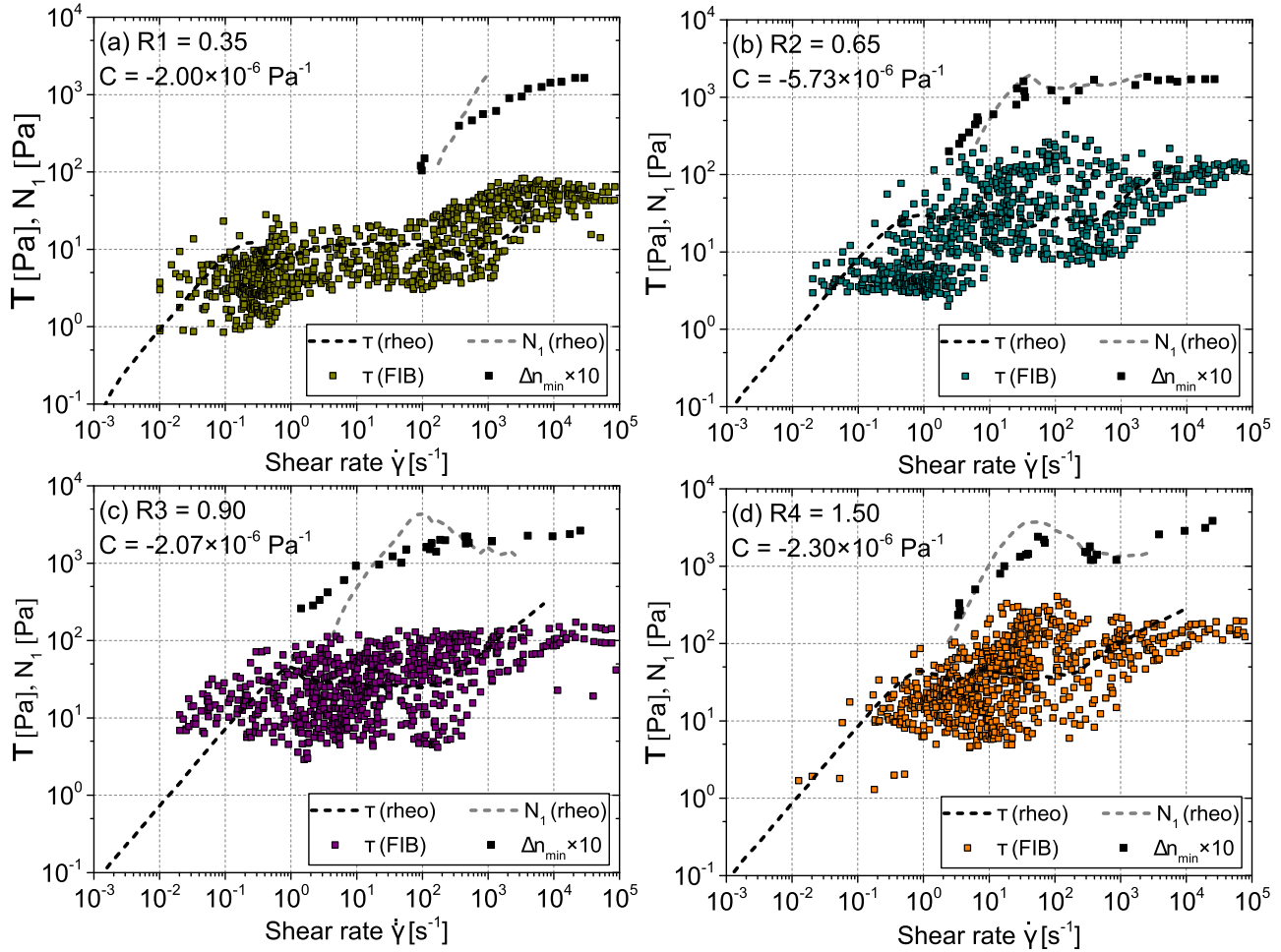
FIG. 8. Determination of the stress-optical coefficient C comparing the local shear stress τ from FIB measurements and the local shear rate from μPIV. For comparison, the dashed lines represent the bulk rheological measurements from Fig. 3(b). Empirically it was observed that the values of Δn_{min} (black squares) correlate to the first normal stress difference N_1 if multiplied by a shift factor of 10.

$N_1(\dot{\gamma}) \sim 10\Delta n_{min}(\dot{\gamma})/C$ as indicated in Fig. S1(III-b). It must be noted that this correlation is based on observations and several reasons for the offset might exist: (i) Formation of shear-bands in the xz-plane of the channel or (ii) by the design of the optical train probing the birefringence signal across the entire channel thickness. The local shear stresses as a function of y and flow rate Q are shown in Fig. 9 as colormaps. The comparison of Fig. 6 to Fig. 9 indicates that similar distributions of shear rate (from μPIV) and shear stress (from FIB) as a function of the flow rate occur for completely independent measurements. In both cases, the maximum values occurred near the walls, while the center of the channel has values close to zero, as expected. We estimate the position along y, where the interface between the shear bands occurs. According to Masselon *et al.* [21], the interface should be located where the stress plateau τ_p is reached. In Fig. 9, we indicate the values of τ_p, which are all in the green region of the colorbar. We observe that the position of the interface varies with flow rate and salt content. In literature, two methods are reported to estimate the high shear-band width near a wall l_{sb}: (i) The slope change of the velocity profile near the channel walls [20], and (ii) using $l = \langle U \rangle / \dot{\gamma}_2$ [22]. If the latter is considered for our solutions, shear band width increases with salt addition (inversely

proportional to $\dot{\gamma}_2$ in Table S1), and R3 and R4 are expected to have similar band widths. Figure 9(a) exhibits a thin high stress region near the walls for R1, until $Wi \approx 130$, when shear-banding ends and parabolic profiles develop. This limit is indicated by the dashed line Q_1. For R2, the high shear-band region near the wall is hardly seen for $Q < Q_2$ in Fig. 6(b). However, this region is very pronounced in the FIB measurements in Fig. 9(b). The striations previously discussed for WLMs R3 and R4 are observed in Fig. 9(c) as measurement noise for $Q < Q_3$ for R3. The high salt solution, R4, has a high shear stress region near the walls within the shear-banding regime. This instability follows the peak observed in the mean retardance values in Fig. 7(a).

3. Bulk versus microfluidic rheology

The local viscosity in the microfluidic channel was calculated by $\eta(Q, y) = \tau(Q, y)/\dot{\gamma}(Q, y)$, as shown by the colormaps in Fig. 10, in which only viscosity values lower or equal to the initial zero-shear viscosity of the solutions $\eta_0 \approx 100$ Pa s were considered. Figure 10(a) exhibits the local viscosity along y as a function of increasing flow rates for the linear WLM solution R1. After the shear-banding region ends at $\dot{\gamma}_2$, represented by Q_1 (dashed line), parabolic-like flow profiles are developed and the decrease in viscosity
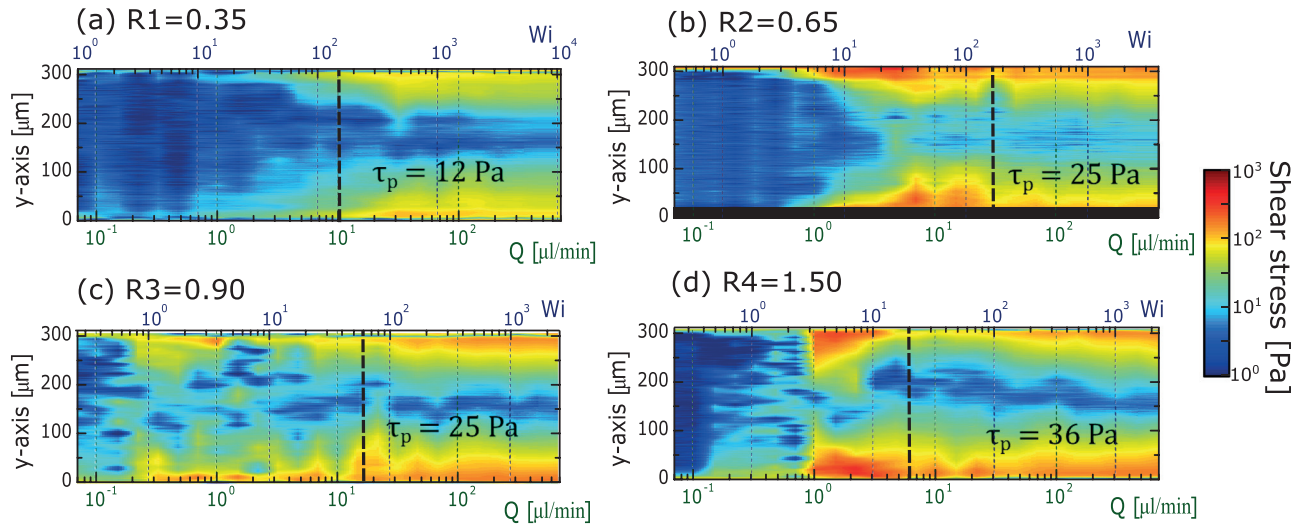
FIG. 9. Determination of local shear stress as a function of y and flow rate $\tau(Q, y)$ determined from FIB measurements. The stress plateau τ_p is shown for comparison. The dashed lines represent the values for Q_x determined in Fig. 6.

near the walls occurs in a uniform and symmetric manner. This is attributed to the growth of high shear-bands with increasing flow rates. The same is observed for the other linear WLMs, the R2 solution. In both cases, we observe that this transition from banded (pluglike) to uniform (parabolic-like) flow profiles occurs for $Wi \approx 200$. A different behavior is observed for the assumed branched WLMs. For these solutions, such a transition does not occur immediately after $\dot\gamma_2$ is reached, instead the high shear-band near the wall is more pronounced even at higher Q, and the same transition to parabolic flow profiles only occurs for $Wi > 1000$.

Combining rheological and spatially resolved SANS, it was confirmed that shear-banding in concentrated WLM solutions depends on shear-induced isotropic to aligned transition [24,40,48]. In the case of semidilute samples, Gurnon *et al.* [18] reported the co-existence of highly aligned WLMs (in the low viscosity band) and isotropic WLMs (in the high viscosity band). The local viscosity displayed in Fig. 10 follows

the latter reference, in which low-viscosity bands are formed at the high shear rate region by the walls (Fig. 6). This is related to highly aligned WLMs, observed from the retardance measurements (Fig. 9). Both entangled and branched WLM systems exhibit shear-banding [51], although their origins differ. Branched WLMs shear-band due to shear-induced demixing of the high shear-band, resulting in a highly branched gel, coexisting in equilibrium with a dilute brine phase [52]. This mechanism differs from the isotropic-aligned phase transition observed for linear WLMs.

In Fig. 11, we reconstruct a master flow curve, representing the local viscosity from Fig. 10 as a function of the local shear rate from Fig. 6. Here, for each flow rate, we have the equivalent shear rate measurements along the y-dimension of the channel from μPIV, as well as the shear stress from FIB measurements. We show that the viscosity profiles in Fig. 10 collapsed into a master flow curve, correlating to the bulk rheology, measured in a rotational rheometer (see dashed
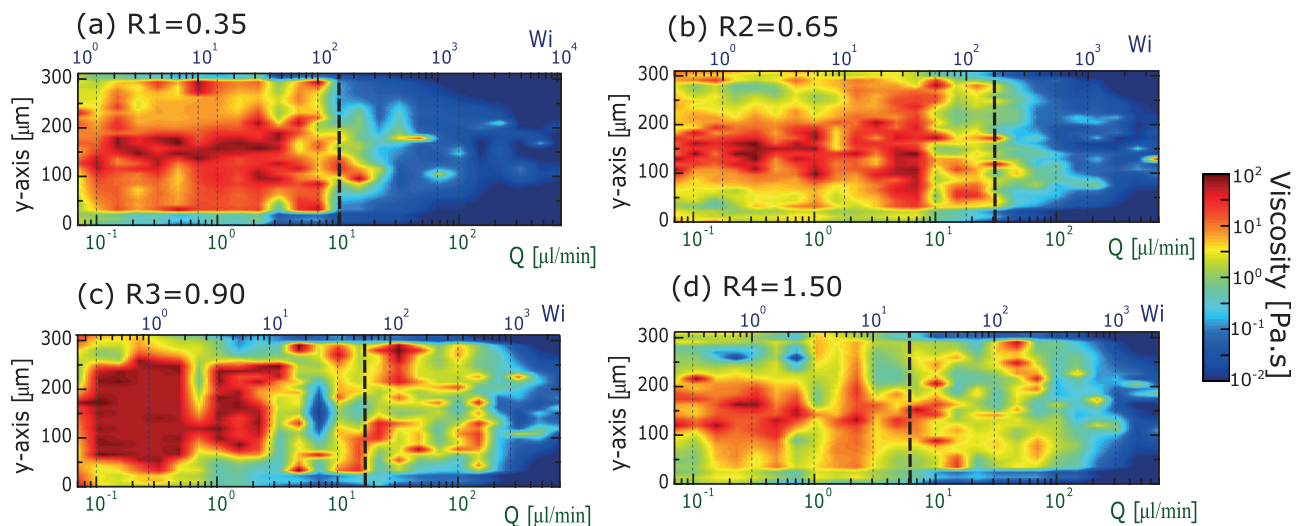

FIG. 10. Calculated local viscosity as a function of y and flow rate $\eta(Q, y)$. The local shear rate is obtained from the μPIV measurements shown in Fig. 6. The local shear stress is obtained from FIB measurements in Fig. 9, based on the determination of the stress-optical coefficient C. The dashed lines represent the values for Q_x determined in Fig. 6.
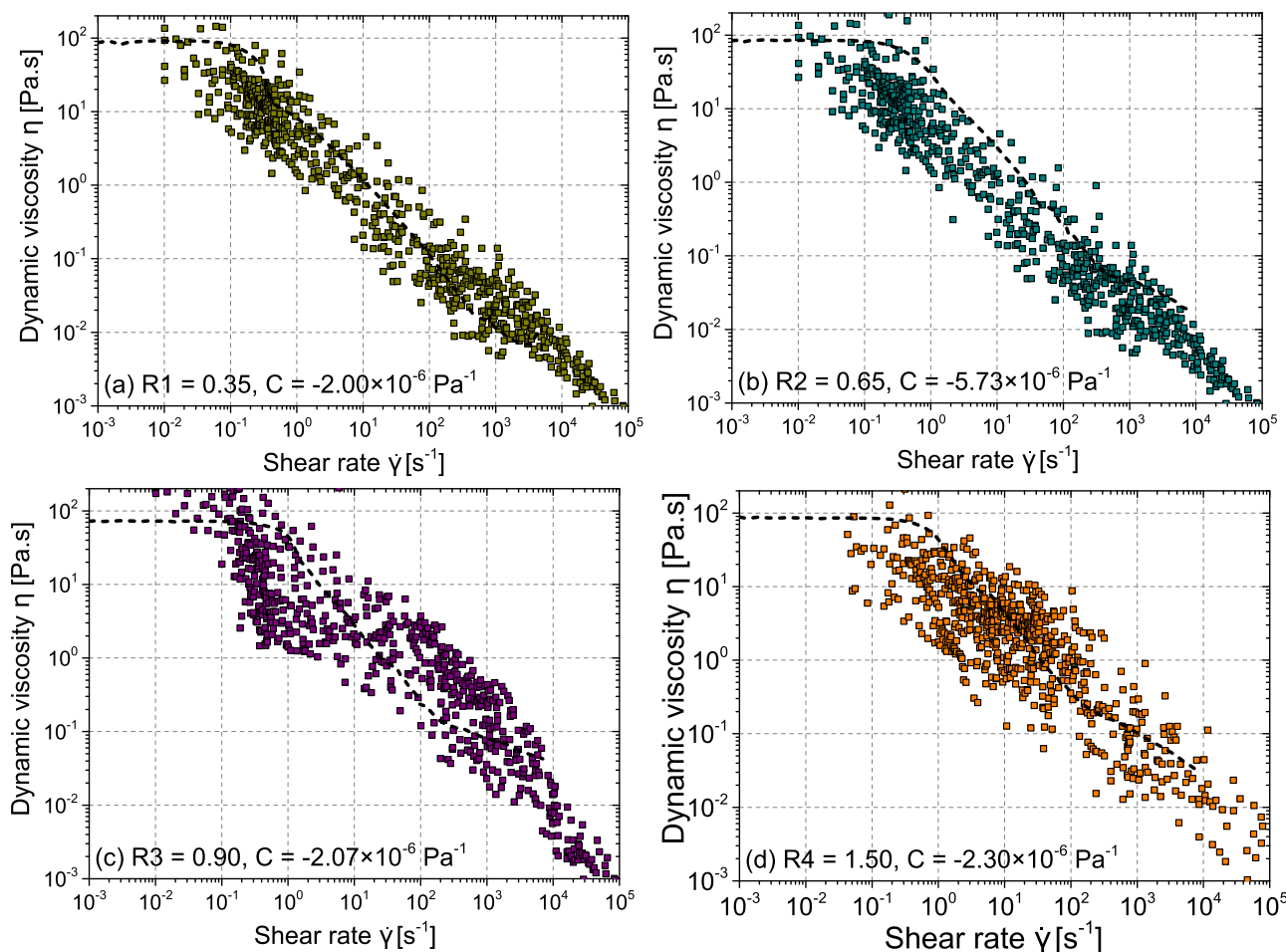
FIG. 11. Master flow curve derived from μPIV and FIB measurements for the different solutions. Notice that no smoothing was performed for the data. For comparison, the dashed lines represent the bulk rheological measurements from Fig. 3(a).

lines). The viscosities in Fig. 11 were not smoothed to demonstrate the divergence between microfluidic flows and the bulk measurement in cone-plate flow-cell. Notice that $\eta(\dot{\gamma}) > 100$ Pa s are present for all solutions in Fig. 11. Especially for R3 [Fig. 11(c)], these points are numerous for low shear rates. This could be caused by the high yield stress which these solutions have, needing longer times to bring the bulk fluid into motion.

IV. CONCLUSION

Four shear-banding surfactant solutions with similar zero-shear viscosities $\eta_0 \approx 100$ Pa s were selected to experimentally compare the influence of structure on the Poiseuille flow developed in straight microfluidic channels. Two parameters are varied based on the sample selection: (i) The electrostatic screening and (ii) the micellar flexibility, both influenced by headgroup structure and salt content. First, we characterize these solutions based on standard oscillatory and rotational rheology with a stress-controlled rheometer. Even though all samples have nearly the same η_0, different rheological responses, due to salt neutralization and changes in micellar structure, were observed. Solution R1 = 0.35 is the least screened micellar solution and showed the most distinct rheological response, either at rest or under flow.

Additionally, we observe that increasing the salt content decreases the extension of stress plateau regions, characteristic of shear-banding solutions. This directly correlates the effect of salt neutralization to the flow-induced transitions occurring in micellar solutions.

To quantify the impact of flow on shear-banding, as well as the interdependence between structure and flow development, a new visualization method was developed. Local shear rate profiles along the y-dimension of a planar microfluidic channel were calculated over a wide range of imposed steady volumetric flow rates Q from μPIV. The non-normalized velocity flow profiles were differentiated to give the local shear rate $\dot{\gamma}(Q, y)$ as shown in Fig. 6. For the same channel and conditions, the local shear stress $\tau(Q, y)$ was derived from spatially resolved measurements of FIB, shown in Fig. 9. The combination of μPIV and FIB measurements provides enough statistics during short acquisition times, thus unsteady shear-banding flows could be observed.

In rheo-optical measurements, the stress-optical rule $\Delta\tau = \Delta n/C$ is often employed to estimate the optical-stress coefficient C, linking birefringence Δn to the principal stress difference $\Delta\tau$. Shear rates and stresses must be zero in the center of a channel with Poiseuille flow. To fulfill such requirement, we normalized our birefringence profiles by its minimum value Δn_{min}, and a correction was applied to the

stress-optical rule $\Delta\tau = (\Delta n - \Delta n_{min})/C$. We observe that Δn_{min} correlates directly to the incite of the first normal stress difference N_1 through $N_1 \sim 10\Delta n_{min}/C$, although the origin of the shift factor is not yet clear. The offset could be related to the formation of shear-bands in the xz-plane of the channel or by the oversampling of the birefringence signal due to the optical train probing the entire channel thickness.

The modified stress-optical rule enabled us to compare shear stresses and normal stresses, calculated by the combination of μPIV and FIB measurements, to bulk rheological measurements, obtained in a rotational rheometer. After such modification, the stress-optical coefficient C was valid for the whole range of shear rates tested, having the same order of magnitude as previous reported values, obtained in Couette flows. To confirm the applicability of such method, a master flow curve was estimated from the local viscosities related to local shear rates. The *in situ* viscosity was calculated based on a simple division of $\eta(Q,y) = \tau(Q,y)/\dot{\gamma}(Q,y)$ as shown in Fig. 10. The values obtained from microfluidic rheology are in agreement with bulk rheology. The higher variability in the stress plateau region indicates the extension of shear-banding and the validity of our method to perform measurements under such unstable conditions.

Our data determined differences in shear-banding behavior caused by structure and salt concentration of surfactant solutions. Structural differences are clear from the rheological measurements and response to imposed stress for linear, entangled WLMs and branched WLMs, indicating that such solutions have morphologies which influence their flow response. This *in situ* determination of rheological properties has many potential applications for the study of complex fluids and flow characterization. The ability of estimating not only the existence but also the development and dimensions of shear-bands in microfluidic flows has a wide range of applications. For example, the challenging measurement of extensional viscosity is one of our next challenges.

ACKNOWLEDGMENTS

References

[1] Berret, J. F., G. Porte, and J. P. Decruppe, "Inhomogeneous shear flows of wormlike micelles: A master dynamic phase diagram," Phys. Rev. E **55**(2), 1668–1676 (1997).

[2] Decruppe, J. P., and A. Ponton, "Flow birefringence, stress optical rule and rheology of four micellar solutions with the same low shear viscosity," Eur. Phys. J. E **10**(3), 201–207 (2003).

[3] Rehage, H., and H. Hoffmann, "Viscoelastic surfactant solutions: Model systems for rheological research," Mol. Phys. **74**(5), 933–973 (1991).

[4] Fischer, P., and H. Rehage, "Non–linear flow properties of viscoelastic surfactant solutions," Rheol. Acta **36**(1), 13–27 (1997).

[5] Cromer, M., L. P. Cook, and G. H. McKinley, "Pressure-driven flow of wormlike micellar solutions in rectilinear microchannels," J. Non-Newtonian Fluid Mech. **166**(3–4), 180–193 (2011).

[6] Lerouge, S., and J. F. Berret, "Shear-induced transitions and instabilities in surfactant wormlike micelles," Adv. Polym. Sci. **230**, 1–71 (2010).

[7] Haward, S. J., F. J. Galindo-Rosales, P. Ballesta, and M. A. Alves, "Spatiotemporal flow instabilities of wormlike micellar solutions in rectangular microchannels," Appl. Phys. Lett. **104**(12), 124101 (2014).

[8] Lutz-Bueno, V., J. Kohlbrecher, and P. Fischer, "Micellar solutions in contraction slit-flow: Alignment mapped by SANS," J. Non-Newtonian Fluid Mech. **215**, 8–18 (2015).

[9] Fardin, M. A., and S. Lerouge, "Flows of living polymer fluids," Soft Matter **10**(44), 8789–8799 (2014).

[10] Cates, M. E., "Reptation of living polymers: Dynamics of entangled polymers in the presence of reversible chain-scission reactions," Macromolecules **20**, 2289–2296 (1987).

[11] Keunings, R., "Micro-macro methods for the multiscale simulation of viscoelastic flow using molecular models of kinetic theory," Rheol. Rev. **2004**, 67–98.

[12] Manneville, S., "Recent experimental probes of shear banding," Rheol. Acta **47**(3), 301–318 (2008).

[13] Cates, M. E., and S. M. Fielding, "Rheology of giant micelles," Adv. Phys. **55**, 799–879 (2006).

[14] Vasquez, P. A., G. H. McKinley, and L. P. Cook, "A network scission model for wormlike micellar solutions. I. Model formulation and viscometric flow predictions," J. Non-Newtonian Fluid Mech. **144**(2–3), 122–139 (2007).

[15] Germann, N., L. P. Cook, and A. N. Beris, "Nonequilibrium thermodynamic modeling of the structure and rheology of concentrated wormlike micellar solutions," J. Non-Newtonian Fluid Mech. **196**, 51–57 (2013).

[16] Berret, J. F., D. C. Roux, and P. Lindner, "Structure and rheology of concentrated wormlike micelles at the shear-induced isotropic-to-nematic transition," Eur. Phys. J. B **5**(1), 67–77 (1998).

[17] Schmitt, V., C. Marques, and F. Lequeux, "Shear induced phase separation of complex fluids: The role of flow-concentration coupling," Phys. Rev. E **52**, 4007–4009 (1995).

[18] Gurnon, A. K., C. López-Barrón, M. J. Wasbrough, L. Porcar, and N. J. Wagner, "Spatially resolved concentration and segmental flow alignment in a shear-banding solution of polymer-like micelles," ACS Macro Lett. **3**(3), 276–280 (2014).

[19] Sato, K., X. F. Yuan, and T. Kawakatsu, "Why does shear banding behave like first-order phase transitions? Derivation of a potential from a mechanical constitutive model," Eur. Phys. J. E **31**(2), 135–144 (2010).

[20] Masselon, C., J. B. Salmon, and A. Colin, "Rheology of wormlike micelles in a microchannel: Evidence of nonlocal effects," AIP Conf. Proc. **1027**, 186–188 (2008).

[21] Masselon, C., A. Colin, and P. Olmsted, "Influence of boundary conditions and confinement on nonlocal effects in flows of wormlike micellar systems," Phys. Rev. E **81**(2), 021502 (2010).

[22] Ober, T. J., J. Soulages, and G. H. McKinley, "Spatially resolved quantitative rheo-optics of complex fluids in a microfluidic device," J. Rheol. **55**(5), 1127–1159 (2011).

[23] Fuller, G. G., *Optical Rheometry of Complex Fluids* (Oxford University, New York, 1995).

[24] Helgeson, M. E., P. A. Vasquez, E. W. Kaler, and N. J. Wagner, "Rheology and spatially resolved structure of cetyltrimethylammonium

bromide wormlike micelles through the shear banding transition," J. Rheol. **53**(3), 727–756 (2009).

[25] Pathak, J. A., and S. D. Hudson, "Rheo-optics of equilibrium polymer solutions: Wormlike micelles in elongational flow in a microfluidic cross-slot," Macromolecules **39**(25), 8782–8792 (2006).

[26] Haward, S. J., and G. H. McKinley, "Stagnation point flow of wormlike micellar solutions in a microfluidic cross-slot device: Effects of surfactant concentration and ionic environment," Phys. Rev. E **85**(3), 031502 (2012).

[27] Lutz-Bueno, V., R. Pasquino, M. Liebi, J. Kohlbrecher, and P. Fischer, "Viscoelasticity enhancement of surfactant solutions depends on molecular conformation: Influence of surfactant headgroup structure and its counterion," Langmuir **32**(17), 4239–4250 (2016).

[28] Lutz-Bueno, V., J. Zhao, R. Mezzenga, T. Pfohl, P. Fischer, and M. Liebi, "Scanning-SAXS of microfluidic flows: Nanostructural mapping of soft matter," Lab Chip **16**, 4028–4035 (2016).

[29] Pipe, C. J., T. S. Majmudar, and G. H. McKinley, "High shear rate viscometry," Rheol. Acta **47**(5–6), 621–642 (2008).

[30] See supplementary material at http://dx.doi.org/10.1122/1.4985379 for detailed information on data analysis, rheological parameters, and additional FIB images.

[31] Meinhart, C. D., S. T. Wereley, and M. H. B. Gray, "Volume illumination for two-dimensional particle image velocimetry," Meas. Sci. Technol. **11**(6), 809–814 (2000).

[32] Lutz-Bueno, V., M. Liebi, J. Kohlbrecher, and P. Fischer, "Intermicellar interactions and the viscoelasticity of surfactant solutions: Complementary use of SANS and SAXS," Langmuir **33**, 2617–2627 (2017).

[33] Lequeux, F., "Reptation of connected worm," Europhys. Lett. **19**(8), 675–681 (1992).

[34] Imae, T., "Spinnability of viscoelastic surfactant solutions and molecular assembly formation," in *Structures Flow Surfactant Solution*, edited by C. A. Herb and R. K. Prudhomme, ACS Symposium Series (ACS, Chicago 1994), pp 140–152.

[35] Oelschlaeger, C., M. Schopferer, F. Scheffold, and N. Willenbacher, "Linear-to-branched micelles transition: A rheometry and diffusing wave spectroscopy (DWS) study," Langmuir **25**(2), 716–723 (2009).

[36] Sachsenheimer, D., C. Oelschlaeger, S. Müller, J. Küstner, S. Bindgen, and N. Willenbacher, "Elongational deformation of wormlike micellar solutions," J. Rheol. **58**(6), 2017–2042 (2014).

[37] Granek, R., and M. E. Cates, "Stress relaxation in living polymers: Results from a Poisson renewal model," J. Chem. Phys. **96**(6), 4758–4767 (1992).

[38] Parker, A., and W. Fieber, "Viscoelasticity of anionic wormlike micelles: Effects of ionic strength and small hydrophobic molecules," Soft Matter **9**(4), 1203–1213 (2013).

[39] Miller, E., and J. P. Rothstein, "Transient evolution of shear-banding wormlike micellar solutions," J. Non-Newtonian Fluid Mech. **143**(1), 22–37 (2007).

[40] Helgeson, M. E., M. D. Reichert, Y. T. Hu, and N. J. Wagner, "Relating shear banding, structure, and phase behavior in wormlike micellar solutions," Soft Matter **5**(20), 3858–3869 (2009).

[41] Dealy, J. M., and J. Wang, *Melt Rheology and its Applications in the Plastics Industry* (Springer, Munich, 2013).

[42] Sharma, V., and G. H. McKinley, "An intriguing empirical rule for computing the first normal stress difference from steady shear viscosity data for concentrated polymer solutions and melts," Rheol. Acta **51**(6), 487–495 (2012).

[43] Colin, A., T. M. Squires, and L. Bocquet, "Soft matter principles of microfluidics," Soft Matter **8**(41), 10527–10529 (2012).

[44] Masselon, C., J. B. Salmon, and A. Colin, "Nonlocal effects in flows of wormlike micellar solutions," Phys. Rev. Lett. **100**(3), 038301 (2008).

[45] Nghe, P., G. Degré, P. Tabeling, and A. Ajdari, "High shear rheology of shear banding fluids in microchannels," Appl. Phys. Lett. **93**(20), 204102 (2008).

[46] Vasudevan, M., E. Buse, H. Krishna, R. Kalyanaraman, A. Shen, B. Khomami, and R. Sureshkumar, "Reversible and irreversible flow-induced phase transitions in micellar solutions," AIP Conf. Proc. **1027**, 976–978 (2008).

[47] Vasudevan, M., E. Buse, D. Lu, H. Krishna, R. Kalyanaraman, A. Shen, B. Khomami, and R. Sureshkumar, "Irreversible nanogel formation in surfactant solutions by microporous flow," Nat. Mater. **9**(5), 436–441 (2010).

[48] Helgeson, M. E., L. Porcar, C. Lopez-Barron, and N. J. Wagner, "Direct observation of flow-concentration coupling in a shear-banding fluid," Phys. Rev. Lett. **105**(8), 084501 (2010).

[49] Lerouge, S., J. P. Decruppe, and J. F. Berret, "Correlations between rheological and optical properties of a micellar solution under shear banding flow," Langmuir **16**(16), 6464–6474 (2000).

[50] Nghe, P., S. M. Fielding, P. Tabeling, and A. Ajdari, "Microchannel flow of a shear-banding fluid: Enhanced confinement effect and interfacial instability," e-print arXiv:0909.1306v1.

[51] Liberatore, M., F. Nettesheim, N. J. Wagner, and L. Porcar, "Spatially resolved small-angle neutron scattering in the 1-2 plane: A study of shear-induced phase-separating wormlike micelles," Phys. Rev. E **73**(2), 020504 (2006).

[52] Thareja, P., I. H. Hoffmann, M. W. Liberatore, M. E. Helgeson, Y. T. Hu, M. Gradzielski, and N. J. Wagner, "Shear-induced phase separation (SIPS) with shear banding in solutions of cationic surfactant and salt," J. Rheol. **55**(6), 1375–1397 (2011).